Stray Light Calibration and Correction of EnMAP's Imaging Spectrometers

Andreas Baumgartner, Claas Henning Köhler, Simon Baur, Richard Wachter, Leonhard Polz, and Anna Serdyuchenko

***Abstract*— We report on the on-ground stray light calibration of the hyperspectral Environmental Mapping and Analysis Program (EnMAP) satellite mission, which was successfully launched into space on April 1, 2022. EnMAP's optical payload consists of a visible and near-infrared (VNIR) (420–1000 nm) and a short wavelength infrared (SWIR) (900–2450 nm) imaging spectrometer. Using a custom-built light source and a collimator, we determined the diffuse stray light by measuring the point spread functions (PSFs) at 12 spatial and 15 (11 VNIR, 4 SWIR) spectral positions with a dynamic range between eight and nine orders of magnitude. Additionally, we measured the out-of-field stray light in along-track direction over an angular range of ±0.2°, resulting in an along-track response function (AltRF) for each spectrometer unit with a dynamic range of $\sim 10^7$. To reduce memory usage and computational time, we use a binned stray light extraction matrix to correct the diffuse stray light. The along-track out-of-field stray light of individual frames is corrected by subtracting preceding and following frames that are weighted with the AltRF. Finally, we show with simulations the impact of both types of stray light on a test scene and evaluate the performance of the presented correction methods in the same manner.**

***Index Terms*— Calibration, Environmental Mapping and Analysis Program (EnMAP), hyperspectral, imaging spectrometer, stray light.**

I. Introduction

THE German imaging spectrometer satellite mission Environmental Mapping and Analysis Program (EnMAP) [1] was launched on April 1, 2022 and has been operational since November 2, 2022 [2]. Its optical payload consists of a visible and near-infrared (VNIR) (420–1000 nm) and a short wavelength infrared (SWIR) (900–2450 nm) imaging spectrometer with a field of view (FOV) of 2.63° and an instantaneous FOV (IFOV) of 9.5 arcsec resulting in a geometric resolution of approximately 30 × 30 m^2.

Prior to the launch, both imaging spectrometers were thoroughly calibrated in the laboratory during EnMAP's calibration and characterization campaign [3], [4]. Here, we report on the diffuse and along-track out-of-field stray light measurements, conducted over a three-week period in November and December 2020, and how we use the results to correct both phenomena. In addition, we also performed checks for ghost images and across-track out-of-field stray light. They confirmed the prediction from simulations that out-of-field stray light is low and ghosts are weak. Therefore, they do not require a correction and are not included in this report.

We define stray light as follows. Each pixel of the detector array of an imaging spectrometer is sensitive to light entering the instrument under certain along-track and across-track angles within a given wavelength range. A nominal pixel is therefore the pixel on which the majority of light is supposed to fall for a given angle of incidence and wavelength. The in-band area extends the nominal pixel area in the direction of the along-track, across-track, and wavelength axes forming the 3-D data space collected by imaging spectrometers. If light originates outside of an instrument's nominal FOV (out-of-field) or outside of its nominal spectral range (out-of-band), it is not supposed to fall on any pixel. Stray light is therefore the light that falls on a pixel that it is not supposed to fall on.

Diffuse stray light originates from diffuse reflections, scattering, or diffraction within an instrument's FOV and spectral range. As such, it is directly related to the nominal measured signal, where it manifests itself in the far wings of the point spread functions (PSFs). Hence, diffuse stray light is widespread and varies slowly with detector location. For a point illumination, the light spread in the PSF wings is usually below the detector's dynamic range. In case of many point illuminations, however, i.e., larger illuminated areas, the sum of light distributed in the PSF wings becomes detectable.

In contrast to diffuse stray light, ghosts are caused by specular reflections within an instrument's FOV and spectral range. Ghosts are also directly related to the nominal measured signal, but within the detector's dynamic range and are located in one or a few pixels.

Along-track stray light is a signal caused by light sources outside the nominal FOV at the time of acquisition, but it passes through the nominal FOV at another point of time as the instrument travels along its orbit.

Similarly, across-track out-of-filed stray light also originates outside the nominal FOV, but it never passes through it at another point in time.

The remainder of this article is structured as follows. We summarize the most relevant properties of the EnMAP spectrometers in Section II, before discussing their respective

Received 23 September 2024; revised 7 February 2025; accepted 12 March 2025. Date of publication 1 April 2025; date of current version 21 April 2025. This work was supported by the German Federal Ministry of Economic Affairs and Energy (BMWi) through the EnMAP project was executed by OHB System AG under contract from the Space Administration unit of Deutsches Zentrum für Luft–und Raumfahrt e.V. (German Aerospace Center–DLR RFM) under Grant 50 EP 0801. DLR-IMF was subcontracted by OHB System AG to support the laboratory characterization and calibration of EnMAP. *(Corresponding author: Andreas Baumgartner.)*

Andreas Baumgartner and Claas Henning Köhler are with the German Aerospace Center (DLR), Remote Sensing Technology Institute (IMF), 82234 Weßling, Germany (e-mail: andreas.baumgartner@dlr.de; claas.koehler@dlr.de).

Simon Baur, Richard Wachter, Leonhard Polz, and Anna Serdyuchenko are with OHB System AG, 82234 Weßling, Germany (e-mail: simon.baur@ohb.de; richard.wachter@ohb.de; leonhard.polz@ohb.de; anna.serdyuchenko@ohb.de).

Digital Object Identifier 10.1109/TGRS.2025.3552114

© 2025 The Authors. This work is licensed under a Creative Commons Attribution 4.0 License.
For more information, see https://creativecommons.org/licenses/by/4.0/

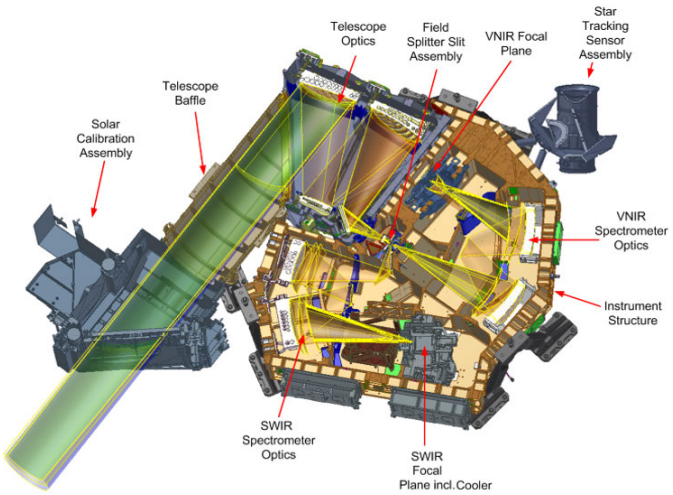

Fig. 1. Optical layout of the EnMAP instrument. In the image plane of the TMA, the FSSA separates the optical beam into the VNIR and SWIR spectrometer units.

stray light requirements in Section III. In Section IV, we give insight into the equipment employed during our measurements. Finally, in Sections V and VI, we describe the measurement, correction, and simulation of the diffuse and along-track stray light, respectively.

II. Environmental Mapping and Analysis Program

EnMAP collects light with a three-mirror anastigmat (TMA) that has an entrance aperture of 18 cm, see Fig. 1. In the image plane of the TMA, the field-splitter and slit assembly (FSSA) [5] separates the focused light with two micro-slits and a micro-mirror into the VNIR and SWIR spectrometer units. This causes a separation of both spectrometers' along-track FOVs by 20 IFOV (∼0.053°). In each of the spectrometer units, four curved prisms in double-pass configuration spectrally disperse the light, which is then imaged through a window on the VNIR and SWIR detectors, respectively.

The most important detector and spectrometer parameters for this work are listed in Table I, where signal values are given in units of digital number (DN). A back-thinned silicon complementary metal-oxide-semiconductor (CMOS) imaging sensor built by Fairchild Imaging is used as the VNIR detector. The SWIR detector manufactured by AIM consists of a mercury cadmium telluride (MCT)-based photon-sensitive array mounted on a readout integrated circuit (ROIC). Both detectors use a global shutter [6], [7].

Although the VNIR and SWIR detectors have a size of 1056 × 256 pixel^2 (spectral channel × spatial column) and 1024 × 288 pixel^2, respectively, only a subset can be read out simultaneously. For standard in-orbit operations, both detectors have a nominal readout area of 1000 spatial columns and 91 (VNIR) or 156 (SWIR) spectral channels. Additional channels and columns were recorded during stray light measurements in order to obtain as much information as possible, as reported in Table I. Unlike the VNIR spectrometer, the SWIR spectrometer has a decreasing wavelength with increasing channel index.

TABLE I
ENMAP Spectrometer and Detector Parameters. LFWC Is the Linear Full Well Capacity. SSD Is the Spectral Sampling Distance. The Saturation Value Is Applicable for High and Low Gain

Parameter	VNIR	SWIR
Detector technology	Silicon CMOS	MCT + ROIC
Electronic shutter	Global	Global
Size [columns]	1056	1024
Size [channels]	256	288
Readout area [columns]	0–4, 20–1035, 1052–1055	0–1024
Readout area [channels]	83–181	62–220
Nominal area [columns]	27–2026	13–2012
Nominal area [channels]	88–178	64–219
Gain ratio [high/low]	5.018 ± 0.033	3.420 ± 0.028
LFWC (low gain) [DN]	6775	11050
LFWC (high gain) [DN]	5508	11260
Saturation value [DN]	7300	15383
Spectral range [nm]	420–1000	900–2450
SSD [nm]	4.7–8.2	7.5–12.0
Spectral resolution [SSD]	<1.25	<1.25
FOV [°]	2.63	2.63
IFOV [arcsec]	9.5	9.5

For the VNIR detector, an etaloning effect, starting around channel 125 (∼600 nm) and increasing with the channel index, was observed during spectral and radiometric calibration [4]. The effect leads to fringing patterns, i.e., high-frequency signal fluctuations, in the measured signal, even if smooth spectra are measured. We expected that the stray light measurements could also be influenced by this effect.

Both detectors have two gain modes: high and low. To convert signal levels from one gain mode to another, we use the fixed gain ratios given in Table I. We performed all measurements that we discuss in this article with the detectors operating in the integrate-then-read (ITR) mode, instead of the standard in-orbit operation of stare-while-scan (SWS) mode, since we expected less detector artifacts during high-intensity measurements.

III. Stray Light Requirements

The development of the stray light measurement and correction presented here is based on requirements formulated with the help of the stray light reference scene depicted in Fig. 2. The scene is defined as an 11 pixel wide region of minimum radiance L_{min}, surrounded by an area with reference radiance L_{ref}, extending to infinity. The expected raw signal levels observed by both imaging spectrometers for the minimum and the reference radiance spectra are calculated from the EnMAP spectral response functions (SRFs) and radiometric responses predicted prior to calibration.

The evaluation point is in the center of the L_{min} region, at which, after correction, the stray light must be either less than 0.5% of the signal level or less than 3 DN in low gain mode. In high gain mode, the signal must be smaller than 15 DN (VNIR) or 11 DN (SWIR). These signal levels are equivalent to the noise level.

For EnMAP, we define the in-band area to be nine pixels wide, i.e., ±4 pixel from each nominal pixel. Choosing an in-band area of this size has the following reasons. A smaller in-band area would cause sharpening of the along-track,

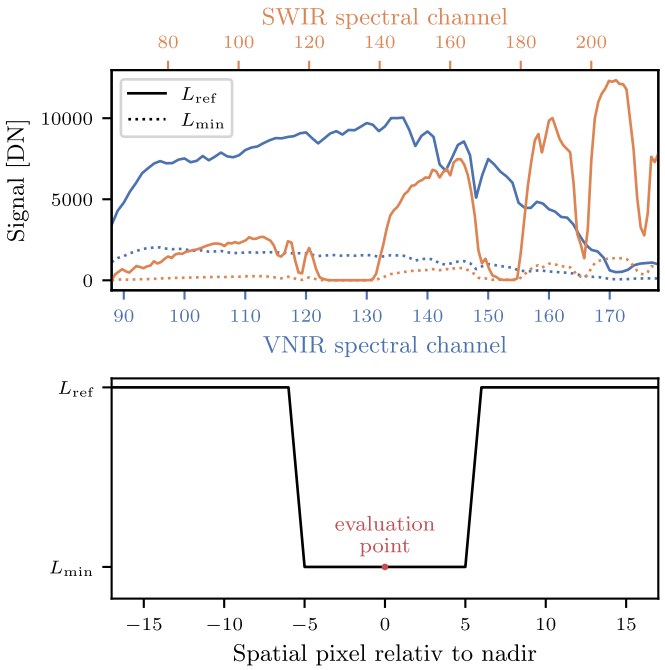

Fig. 2. (Top) EnMAP reference L_{ref} and minimum L_{min} signal for the VNIR and SWIR spectrometers in high gain mode. (Bottom) Stray light reference scene composed of L_{ref} and L_{min} signal. Note that for the SWIR spectrometer, the wavelength decreases as the channel index increases.

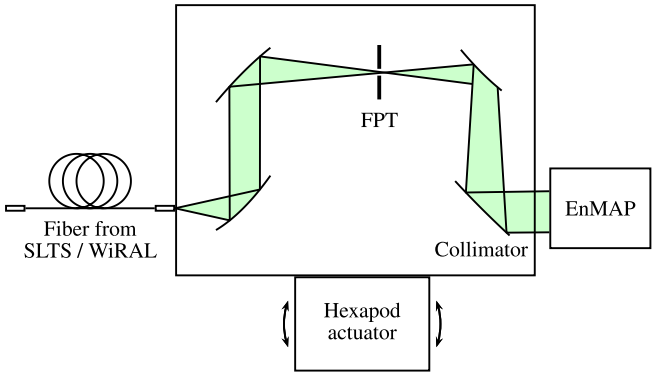

Fig. 3. Schematic drawing of the FAI collimator setup used for EnMAP stray light measurements. Focusing optics image the end of an optical fiber in the focal plane of a collimator, which guides the beam to EnMAP. Different FPTs of different sizes and shapes are available.

across-track, and SRFs, which, in turn, would alter the key instrument parameters and increase noise. At the same time, we wanted to keep the in-band area as small as possible, since stray light effects are limited to the in-band area after correction. Additionally, this allows us to use a binning method with 3×3 pixel^2 tiles for the diffuse stray light correction, see Section V-I.

IV. Measurement Setup

The measurements presented in this article were carried out with either the stray light test source (SLTS) [8], [9] or the wide-range adjustable light source (WiRAL) [10] (a monochromator) coupled into the full-aperture illuminator (FAI) [10] collimator through an optical fiber.

Fig. 3 shows a schematic drawing of the FAI setup. Light from SLTS or WiRAL is guided through an optical fiber into the FAI, where it is focused on a focal plane target (FPT). Several FPTs are available to re-size and shape the image of the fiber. Finally, the beam is collimated to a diameter of 200 mm by two mirrors, which together have a focal length of 2020 mm. The FAI is mounted on a hexapod actuator, which allows the angle of illumination to be varied relative to the instrument. A more detailed description of the EnMAP optical ground support equipment can be found in [3] and [10].

The SLTS is a high-radiance light source that was specifically designed for high dynamic range (HDR) stray light measurements. It can either emit a broadband spectrum or monochromatic light at 15 discrete wavelengths, 11 in the VNIR and four in the SWIR range. High spectral purity with an out-of-band suppression of $\geq 10^9$ is achieved by stacking two to four bandpass filters at each wavelength, see Table II. To control the output intensity, 11 neutral density (ND) filters with nominal optical densities ranging from 0.5 to 5.5 in 0.5 steps are installed in the SLTS. Each ND filter can be combined with every bandpass filter. We calibrated the transmissions of all ND filters in combination with each bandpass filter with an accuracy of 2%. More details about the SLTS can be found in [8].

In contrast to the SLTS, the WiRAL wavelength is freely adjustable, but with lower radiant power and lower spectral purity.

Note that the amount of stray light derived from our measurements should be interpreted as an upper limit to the actual amount of stray light caused by EnMAP's imaging spectrometers, as stray light caused by optical surfaces within the FAI could not be independently characterized. Refer to Section V-E for a discussion how stray light can be attributed to individual optical components in the absence of dedicated characterization measurements on the component level.

V. Diffuse Stray Light

As indicated in Section I, the far wings of the across-track-spectral PSFs are a manifestation of diffuse stray light. Even though stray light caused by illuminating a single pixel (and its surrounding in-band area) is often undetectable due to an instrument's limited dynamic range, the aggregation of stray light through simultaneous illumination of many pixels may cause significant stray light contributions to the measured signal. This explains, why we have to measure the instrument PSFs with a much greater dynamic range than the instrument natively provides.

Therefore, we acquire multiple sub-PSFs at increasing incident intensity, thus gradually overexposing the PSF center while at the same time enhancing the signal level in its wings. The individual sub-PSFs are then combined into a single HDR PSF for each measured pixel.

It is well known that operating detectors far outside the nominal operation conditions during stray light characterization (long exposure times, high detector irradiance) can result in measurement errors due to blooming and electrical crosstalk. Therefore, these effects have been carefully quantified during the detector characterization.

This chapter is structured as follows. Section V-A explains the measurement procedure, while Section V-B provides a

TABLE II
SLTS BANDPASS FILTER CENTER WAVELENGTHS AND BANDPASSES [8]

Filter number	0	1	2	3	4	5	6	7	8	9	10	11	12	13	14
Central wavelength [nm]	450	488	532	590	635	660	730	780	810	850	905	1020	1250	1600	2150
Width of bandpass [nm] @ -80 dB	25	33	25	38	25	25	30	25	25	25	45	32	45	39	62

detailed explanation of the data evaluation process. The obtained VNIR and SWIR spectrometers' PSFs are discussed in Sections V-C and V-D, respectively. A method to estimate the stray light caused by the FAI is described in Section V-E. Section V-F discusses the principal method for stray light correction. In Section V-G, we present an efficient method to calculate the inverse of a stray light matrix. Section V-H outlines an approach to determine a stray light extraction matrix using binned pixels and its application to correct diffuse stray light. The calculation of EnMAP's stray light extraction matrices is detailed in Section V-I, and their application is elaborated in Section V-J. The simulation of stray light effects on the reference scene is described in Section V-K, with the simulation results discussed in Section V-L. Finally, in Section V-M, we address the uncertainties associated with the stray light correction.

A. Diffuse Stray Light PSF Measurements

The diffuse stray light is measured with the SLTS attached to the FAI using a rectangular FAI FPT with a size of 2 × 2 EnMAP IFOV^2. PSFs are acquired at 12 spatial positions evenly distributed across the detector arrays. We measure the VNIR PSFs with SLTS bandpass filters 0–10 and the SWIR PSFs with filters 11–15. 1000 frames are averaged per measurement to guarantee a high signal-to-noise ratio (SNR) and a corresponding dark measurement is taken with the SLTS shutter closed. Every HDR PSF is a composition of eight sub-PSFs, each recorded with a different combination of gain, integration time, and ND filter. The lowest intensity is always chosen so that the center of the PSF is well resolved with the native dynamic range of the detector.

B. Diffuse Stray Light PSF Evaluation

To obtain from the measurement data HDR PSFs, we apply the following steps on each sub-PSF.

1) Average frames of each sub-PSF (including dark frames).
2) Apply nonlinearity correction (including dark frames).
3) Apply response non-uniformity (RNU) correction on all averaged frames (including dark frames).
4) Mask bad pixels.
5) Mask saturated pixels.
6) Mask all pixels next to the pixels masked in the previous step, due to blooming.
7) Mask pixels above the linear full well capacity (LFWC) due to nonlinearity.
8) Remove averaged dark signal.
9) Mask pixels with average signal below the following values:

Sub-PSF	1	2	3	4	5	6	7	8
min VNIR signal [DN]	2	2	2	2	10	10	20	25
min SWIR signal [DN]	1	1	1	1	6	6	12	12.

10) Mask pixels with SNR below

Sub-PSF	1	2	3	4	5	6	7	8
min VNIR SNR	10	10	10	10	10	10	10	10
min SWIR SNR	5	5	5	5	5	10	10	10.

11) Normalize sub-PSF by scaling value (product of the gain ratio (see Section II), integration time, and ND-filter transmission).

We match the sub-PSFs by using scaling values based on the gain ratio, integration times, and ND-filter transmissions to minimize the influence of nonlinear detector responses. After these steps, the sub-PSFs are combined into an HDR-PSF. The highest absolute signal is chosen where more than one measurement exists for any given sampling node of the combined PSF. Missing data values in the PSFs, e.g., due to bad pixels, are then linearly interpolated from adjacent pixels. We continue by determining the sub-pixel position of each PSF by fitting a Gaussian convolved with a rectangular function and shift then the PSF centers to the nearest pixels using linear interpolation. Finally, we normalize each PSF to its in-band region.

The minimum signal and SNR are set to lower values for the first sub-PSFs to obtain data for some pixels in the steep wings of the PSFs, where linear interpolation is less accurate. Since we chose later anyway the sub-PSF data with the highest unmasked signal, only isolated pixels are affected. The influence on the accuracy of the PSFs is negligible, since these pixels have a small relative signal and are mainly located in the in-band area, which is used for PSF normalization but not correction.

Another common method of aligning the sub-PSFs is to match the overlap of the sub-PSF wings instead of scaling them as described. However, this has the disadvantage that nonlinear effects have an exponential impact that increases with the number of sub-PSFs used.

C. VNIR PSF Results

We derived all VNIR PSFs with a dynamic range of eight orders of magnitude or more. In Fig. 4(a), (b), (d), and (e), the measured and VNIR sub-PSFs at spatial column 480 spectral channel 102 before and after normalization are shown. An overview of the PSFs measured with bandpass filter 1 is shown in Figs. 4(c) and 5. In addition, the PSFs measured at spatial column 480 are depicted in Figs. 4(f) and 6.

Two rectangular-shaped patterns are apparent in Figs. 5 and 6: the first pattern is centered on the peak of the PSFs and a second pattern centered along the spatial axis is shifted toward higher channel index numbers. On top

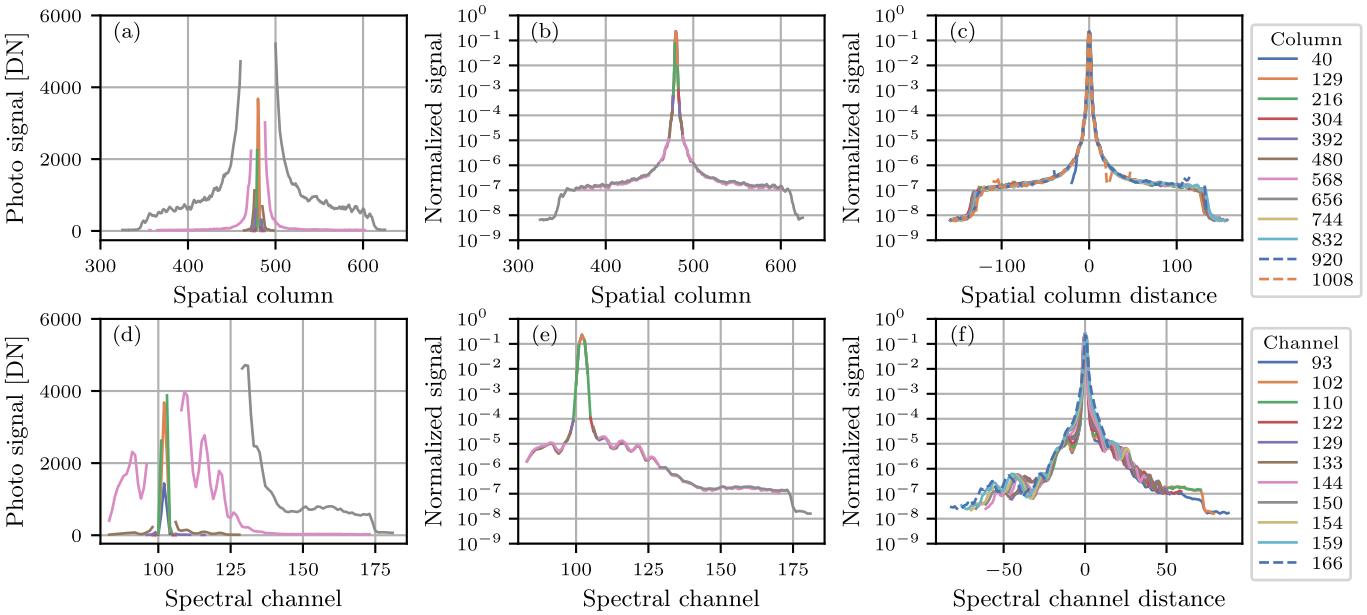

Fig. 4. (a), (b), (d), and (e) VNIR spectrometer sub-PSF at column 480 and channel 102 (a) and (d) before and (b) and (e) after normalization, with slice through the PSF center along (a) and (b) the spatial and (d) and (e) the spectral axis. Different colors represent the different sub-PSFs used to build the full PSF. (c) and (f) Slices through the full VNIR spectrometer PSFs, where their centers are shifted to 0. (c) Slice through the spatial axis of all PSFs measured with bandpass filter 1. (f) Slice through the spectral axis of all PSFs measured at spatial column 480.

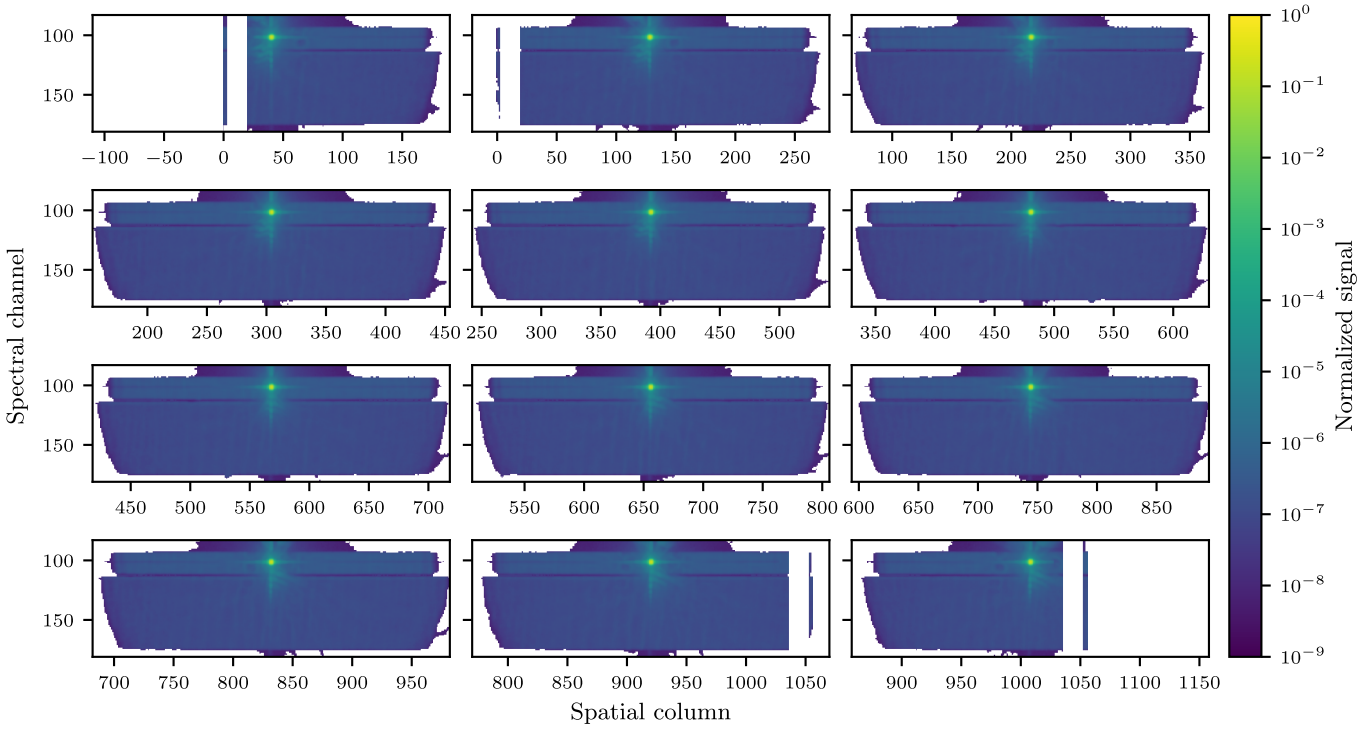

Fig. 5. Overview of VNIR spectrometer PSFs measured with bandpass filter 1. The PSFs at the detector edge are cropped, since they fall partly outside the detector or on pixels that were not recorded. In most outer PSFs (upper left and lower right), additional strips are visible. These are pixels that are read out additionally to the pixels in the nominal illuminated area.

of those shapes, a third pattern slowly changes with across-track pixel index is visible. The width of the PSFs increases with the channel index and therefore with the wavelength, see Fig. 6. Hence, the stray light increases with the channel index, while it is stable along the spatial axis, see Fig. 5.

Although expected, we cannot observe an influence of the etaloning effect on PSF shapes. However, there are some fluctuations in the PSF wings along the spectral axis, but at a lower frequency than the etaloning effect [4], and these fluctuations also occur in channels not affected by etaloning.

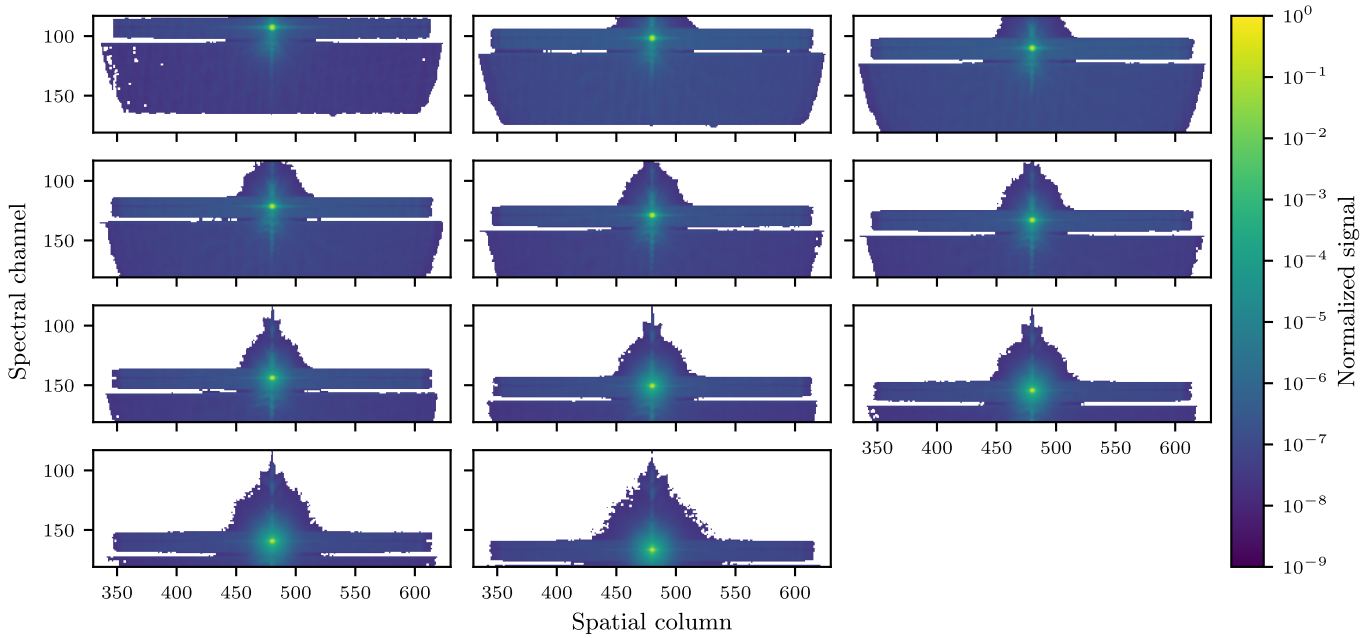

Fig. 6. Overview of VNIR spectrometer PSFs measured at spatial column 480 with bandpass filters 0–10 (from upper left to lower right). For easier comparison, the PSFs are capped to a minimum relative signal of 2.0×10^{-8}.

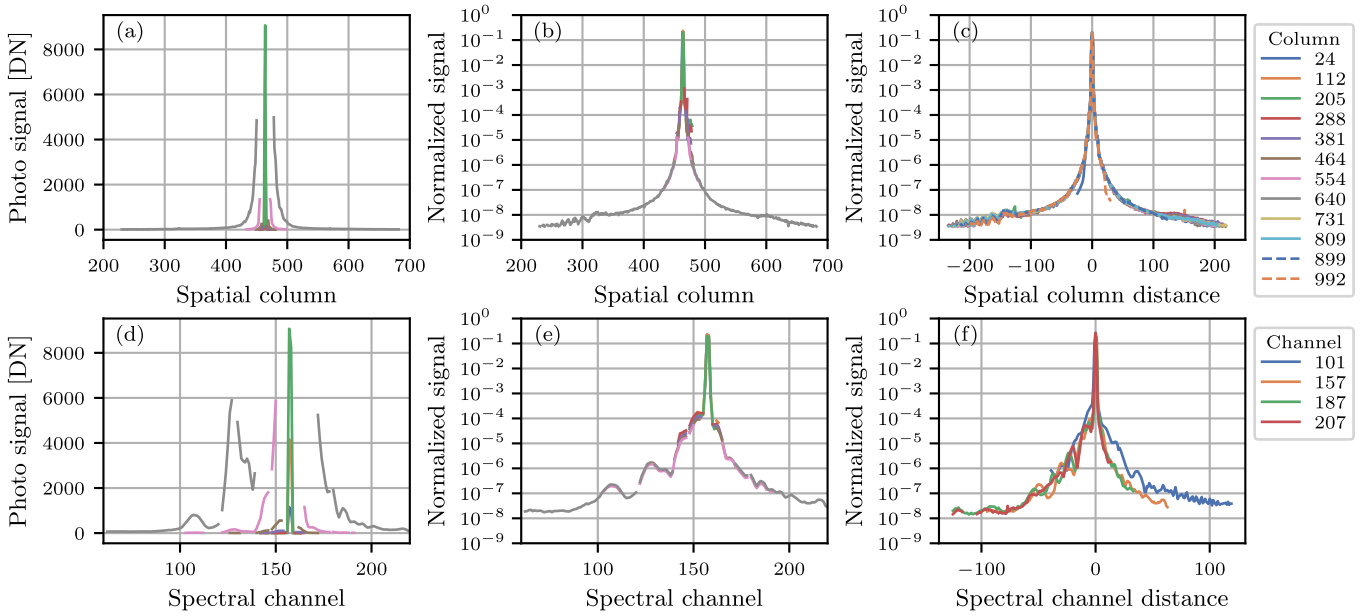

Fig. 7. (a), (b), (d), and (e) SWIR spectrometer sub-PSFs at column 464 and channel 157 (a) and (d) before and (b) and (e) after normalization. The slices are through the PSF center along (a) and (b) the spatial and (d) and (e) the spectral axis. Different colors represent the different sub-PSFs used to build the full PSF. (c) and (f) Slices through the full SWIR spectrometer PSFs, where their centers are shifted to 0. (c) Slice along the spatial axis of all PSFs measured with bandpass filter 13. (f) Slice along the spectral axis of all PSFs measured at spatial column 464. Note that for the SWIR spectrometer, the wavelength decreases as the channel index increases.

D. SWIR PSF Results

Fig. 7(a), (b), (d), and (e) shows the measured and scaled SWIR sub-PSFs at spatial column 464 and spectral channel 157. All derived PSFs have a dynamic range of $\geq 10^8$. In Fig. 7(b), on the right wing of the slice along the spatial axis, some sub-PSFs deviate significantly at some pixels. The same is visible in Fig. 7(e) at lower channel index numbers along the spectral axis. This is caused by a pedestal offset, which has been identified as a detector artifact that so far has only been observed in the non-operational ITR mode of the detector. However, the impact on the derived PSFs is only minor, since the offset stays fixed and the influence of the effect decreases therefore with increasing signal levels.

Figs. 7(c) and 8 show an overview of the PSF measured with bandpass filter 13. In addition, Figs. 7(f) and 9 depict the PSFs measured at spatial column 464. As for the VNIR spectrometer, a pattern is visible that changes with the spatial column of the illumination spot. Otherwise, the principal shape of the PSFs remains stable. The left and right outermost measured PSFs have a reduced dynamic. It seems that the

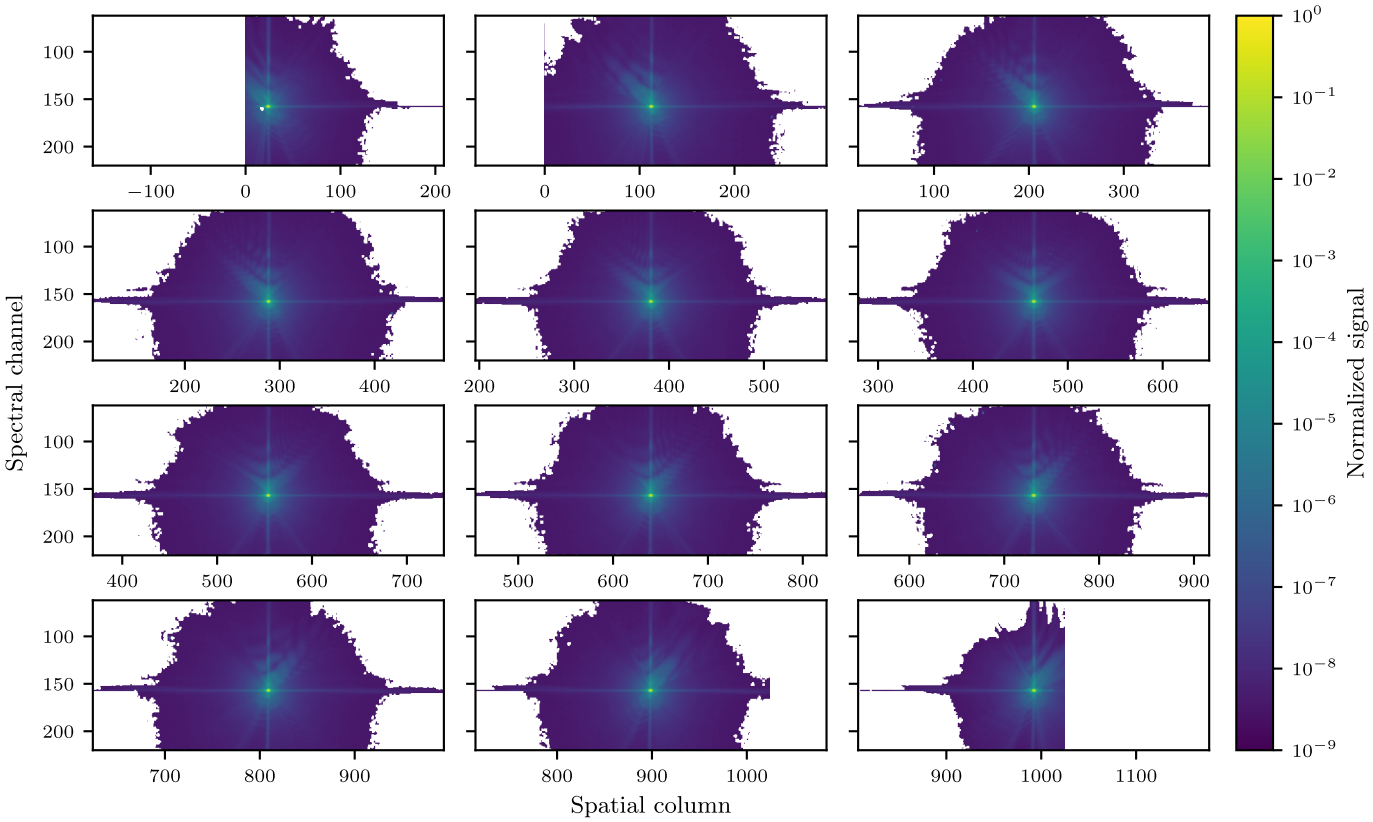

Fig. 8. Overview of SWIR spectrometer PSFs measured with a bandpass filter 13. Note that for the SWIR spectrometer, the wavelength decreases as the channel index increases.

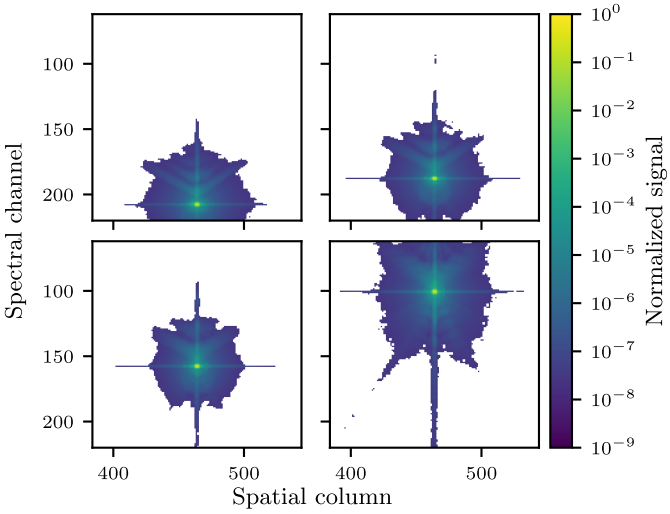

Fig. 9. Overview of SWIR spectrometer PSFs measured at spatial column 464 with bandpass filters 11–14 (from upper left to lower right). Note that for the SWIR spectrometer, the wavelength decreases as the channel index increases. For easier comparison, the PSFs are capped to a minimum relative signal of 2.4×10^{-8}.

instrument is less sensitive there. The intensity settings for the sub-PSF measurements were therefore not scaled in a manner that a complete PSF can be reconstructed. This is visible in Fig. 8 at the outermost PSFs (top left and lower right), where missing information near the center is represented by white pixels. It would be possible to interpolate the missing parts using the next fully measured (without gaps near the center) PSFs in the same channel. However, since the PSF shapes remain almost identical and due to the limited dynamic range, we decided to directly use the gapless PSFs in place of the incomplete ones for further processing. Along the spectral axis, the width of the PSFs is smallest at the center of the detector and increases toward its edges.

E. Estimation of FAI Stray Light

Investigating the most outer spatially positioned PSFs of both detectors, we can see a sudden drop in the PSF shapes along the spatial axis, see Fig. 10(a) and (d). The edge of the drop is located at the edge of the nominal illumination area of the detector, where the across-track illumination region is defined by the short edges of the FSSA slits. This means that any light that falls on the pixels outside the nominal illumination area is stray light. Further, any spatial stray light caused by the TMA and the FAI is also cut off by the slits. Hence, any stray light visible in this region must originate from or after the FSSA. Although stray light originating from or after the FSSA expands in the spatial and spectral dimension, for simplicity, we refer to stray light that emerges before the FSSA as spatial stray light in the following.

We can observe that the signal on the spatial PSF axis caused by spatial stray light, i.e., same channels as nominal illumination spot, is similar to the signal of the adjacent channels. This allows us to estimate the portion of the PSF that originates after the FSSA by linearly interpolating the

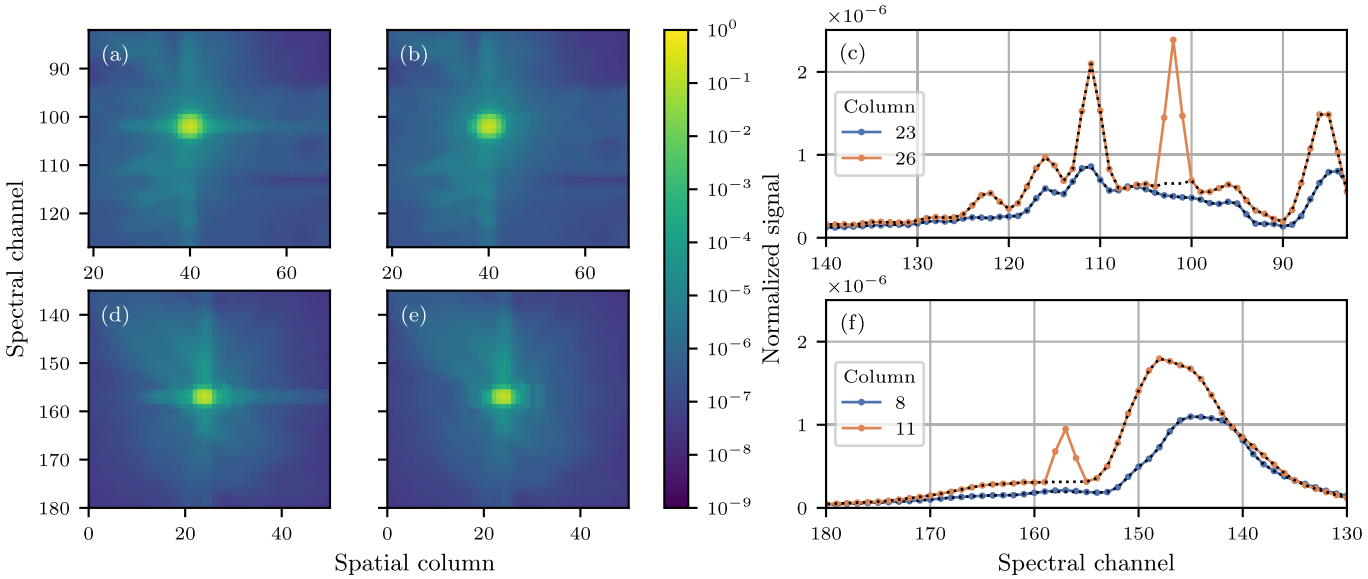

Fig. 10. (a)–(c) Close-ups and slices of the VNIR PSF at column 40 channel 102. (d)–(f) Close-ups and slices of the SWIR PSF at column 24 channel 157. (a) In VNIR channels 101-103, the stray light caused by the TMA and FAI is visible, which is cut around column 24. (d) In SWIR channels 156–158, the stray light caused by the TMA and FAI is visible, which is cut around column 10. (b) and (e) Same PSFs as in (a) and (d) but with TMA and FAI stray light removed. (c) Slices through the VNIR PSF at spatial columns 23 and 26. (f) Slices through the SWIR PSF at spatial columns 8 and 11. Solid lines depict the measured PSF, while dotted lines represent the PSFs without TMA and FAI stray light. Note that for the SWIR spectrometer, the wavelength decreases as the channel index increases.

signal from the adjacent channels outside the in-band area, see Fig. 10(b), (c), (e), and (f).

The spatial stray light is therefore the sum of the FAI and TMA stray light. While with the acquired data, the FAI stray light cannot be separated from TMA stray light, we can use this information to derive an upper boundary for the FAI stray light contribution. Using the interpolation technique described above, we calculate three different PSF types.

1) PSFs with 100% spatial stray light. This would be the correct PSFs if all spatial stray light is caused by the TMA.
2) PSFs with 0% spatial stray light. This would be the correct PSFs if all spatial stray light is caused by the FAI.
3) PSFs with 50% spatial stray light. This is the mean of the previous PSF types. This would be the correct PSFs if spatial stray light is equally caused by the FAI and TMA.

We use the type 3 PSFs for the further processing because it balances the risk of overcorrecting stray light with an insufficient correction of true stray light. This approach is valid because the observed spatial stray light is low and only a relatively small correction is performed.

F. Diffuse Stray Light Correction Method

We follow the approach outlined in [11] for the diffuse stray light correction. For the reader's convenience, we summarize its essential ideas in the following paragraphs. Additionally, we discuss the inversion of the stray light distribution function (SDF) matrix in a little more detail.

Since the PSFs of an instrument are usually not constant and change with detector location, we require for each pixel an individual PSF to describe an instrument. To formalize this, we use the PSF matrix P_{ij}, which describes the relative response of each pixel i caused by an excitation falling on pixel j.

Please note that we assume here that all PSFs are centered on their nominal pixel. This is actually not well-defined as we have argued in [12]. While not valid in general, this is a fair approximation in the context of stray light correction, because we are only interested in the far wings of the PSF, which vary slowly from pixel to pixel.

Since each detector pixel has a distinct PSF, we require an $M \times M$ PSF matrix $\boldsymbol{P}$ to model an instrument with M detector elements. We would like to point out that we do not distinguish here between spectral channels and spatial columns and assign a single index to each detector element.

As instruments are often designed to distribute an ideally collimated and monochromatic beam over several pixels, we use a set IB_j to collect the indices of all pixels within the in-band area of pixel j. Any signal recorded by a pixel in IB_j under an illumination of pixel j is not considered stray light. This idea is formalized in [11] with the introduction of the $M \times M$ SDF matrix $\boldsymbol{D}$

$$D_{ij} := \begin{cases} P_{ij} / \sum_{i \in \mathrm{IB}_j} P_{ij} & \text{for } i \notin \mathrm{IB}_j \\ 0 & \text{for } i \in \mathrm{IB}_j. \end{cases} \tag{1}$$

Note that the stray light caused by each pixel j is normalized with the integrated signal (energy) of all its in-band pixels in $\boldsymbol{D}$. Introducing M-dimensional signal vectors $\boldsymbol{y}_{ib}$ for the in-band signal (without stray light) and $\boldsymbol{y}_{sl}$ for the stray light, we can write

$$\boldsymbol{y}_{sl} = \boldsymbol{D} \cdot \boldsymbol{y}_{ib}. \tag{2}$$

Using the measured signal $\boldsymbol{y}_{meas}$

$$\boldsymbol{y}_{meas} := \boldsymbol{y}_{ib} + \boldsymbol{y}_{sl}. \tag{3}$$

We can eliminate $\boldsymbol{y}_{\mathrm{sl}}$ from (2)

$$\boldsymbol{y}_{\mathrm{meas}} = [\boldsymbol{I} + \boldsymbol{D}] \cdot \boldsymbol{y}_{\mathrm{ib}} \tag{4}$$

where $\boldsymbol{I}$ is the identity matrix.

If the condition number of the matrix $[\boldsymbol{I} + \boldsymbol{D}]$ is close to 1, then a numerically stable solution for the inversion exists and the following equation holds:

$$\boldsymbol{y}_{\mathrm{ib}} = [\boldsymbol{I} + \boldsymbol{D}]^{-1} \cdot \boldsymbol{y}_{\mathrm{meas}}. \tag{5}$$

G. Stray Light Matrix Inversion

Calculating the matrix inversion in (5) faces two problems. First, the matrix is very large, and second, it is not obvious that the inverse exists at all.

To address these issues, we use a result from linear algebra. The equation

$$[\boldsymbol{I} - \boldsymbol{T}]^{-1} = \sum_{k=0}^{\infty} \boldsymbol{T}^k \tag{6}$$

holds for any bounded linear operator $\boldsymbol{T}$ on a normed vector space. The right-hand side of (6) is often called the Neumann series of the operator $\boldsymbol{T}$, see, e.g., chapter 21.5 in [13]. With $\boldsymbol{T} := -\boldsymbol{D}$, it thus remains to show that $\|\boldsymbol{T}\| = \|\boldsymbol{D}\| < 1$ for an arbitrary matrix norm induced by a norm of the associated vector space $\mathbb{R}^M$. Using the 1-norm, we obtain

$$\|D\|_1 = \max_{1 \le j \le M} \sum_{k=0}^{\infty} |D_{kj}| \tag{7}$$

$$= \max_{1 \le j \le M} \sum_{k \notin \mathrm{IB}_j} D_{kj} \tag{8}$$

$$= \max_{1 \le j \le M} \frac{\sum_{k \notin \mathrm{IB}_j} P_{\mathrm{ij}}}{\sum_{k \in \mathrm{IB}_j} P_{\mathrm{ij}}}. \tag{9}$$

In other words, the inverse exists and it can be computed by (6) if the in-band area IB_j for every pixel j is chosen such that it contains more energy than the pixel creates as stray light. This requirement should hold for any decent instrument and it can always be met by a suitable choice of the in-band area. Inverting (4) followed by the insertion of (6) finally yields the stray light corrected signal:

$$\boldsymbol{y}_{\mathrm{ib}} = \left[\boldsymbol{I} - \boldsymbol{D} + \boldsymbol{D}^2 - \ldots\right] \cdot \boldsymbol{y}_{\mathrm{meas}}. \tag{10}$$

The infinite series in square brackets can be used to correct all measurements acquired with a given instrument and thus has to be computed only once. It can usually be truncated after a few terms, as the entries in $\boldsymbol{D}$ are typically quite small.

H. Binned Stray Light Extraction Matrix

For the operational EnMAP processor, it was decided to implement a binned version of the stray light correction instead of computing (5) directly to reduce the processing time and memory usage. This approach is physically justified as diffuse stray light does not change abruptly between adjacent pixels.

To formalize this approach, we define $\bar{M}$ bins $\mathcal{B}_j$ containing the indices of the detector pixels in bin j. The bins may not overlap, i.e., each detector pixel is part of one and only one bin ($\mathcal{B}_i \cap \mathcal{B}_j = \emptyset$ for $i \neq j$). We then define an $\bar{M} \times M$ binning matrix $\boldsymbol{B}$

$$B_{\mathrm{ij}} := \begin{cases} 1 \text{ if } j \in \mathcal{B}_i \\ 0 \text{ else.} \end{cases} \tag{11}$$

Note that the sum over each row i equals the number of detector pixels n_i in the respective bin

$$n_i := \sum_{j=1}^{M} B_{\mathrm{ij}} = |\mathcal{B}_i|. \tag{12}$$

It is straightforward to show that the matrix $\boldsymbol{B}^+$ defined by

$$B^+_{\mathrm{ij}} := \frac{B_{\mathrm{ji}}}{n_j} \tag{13}$$

is the Moore–Penrose pseudo-inverse of $\boldsymbol{B}$. It basically inverts the binning by assigning an equal fraction of the bin's value to each of its elements. Using this notation, we can express the assumption that stray light varies smoothly as follows:

$$\boldsymbol{y}_{\mathrm{sl}} \approx \boldsymbol{B}^+ \cdot \bar{\boldsymbol{y}}_{\mathrm{sl}} = \boldsymbol{B}^+ \bar{\boldsymbol{D}} \boldsymbol{B} \cdot \boldsymbol{y}_{\mathrm{ib}} = \boldsymbol{B}^+ \boldsymbol{B} \boldsymbol{D} \boldsymbol{B}^+ \boldsymbol{B} \cdot \boldsymbol{y}_{\mathrm{ib}} \tag{14}$$

where $\bar{\boldsymbol{y}}_{\mathrm{sl}}$ is the binned stray light vector and $\bar{\boldsymbol{D}}$ is the $\bar{M} \times \bar{M}$ binned stray light matrix. In other words, binning and then expanding the stray light computed from a binned in-band signal yields approximately the same result as computing the stray light from the in-band signal in full resolution.

Insertion of this approximation into (3) yields

$$\boldsymbol{y}_{\mathrm{ib}} = \boldsymbol{y}_{\mathrm{meas}} - \boldsymbol{y}_{\mathrm{sl}} \tag{15}$$

$$\approx \boldsymbol{y}_{\mathrm{meas}} - \boldsymbol{B}^+ \cdot \bar{\boldsymbol{y}}_{\mathrm{sl}} \tag{16}$$

which means that we can correct for stray light using an initially binned stray light vector. We can calculate this vector by inserting (5) in (3)

$$\bar{\boldsymbol{y}}_{\mathrm{sl}} = \bar{\boldsymbol{y}}_{\mathrm{meas}} - \left(\boldsymbol{I} + \bar{\boldsymbol{D}}\right)^{-1} \cdot \bar{\boldsymbol{y}}_{\mathrm{meas}} \tag{17}$$

$$= \left[\boldsymbol{I} - \left(\boldsymbol{I} + \bar{\boldsymbol{D}}\right)^{-1}\right] \cdot \bar{\boldsymbol{y}}_{\mathrm{meas}} \tag{18}$$

where $\bar{\boldsymbol{y}}_{\mathrm{meas}}$ is a binned measurement, defined as

$$\bar{\boldsymbol{y}}_{\mathrm{meas}} := \boldsymbol{B} \cdot \boldsymbol{y}_{\mathrm{meas}}. \tag{19}$$

The last result can be implemented conveniently, as it allows us to define the $\bar{M} \times \bar{M}$ stray light extraction matrix $\bar{\boldsymbol{E}}$

$$\bar{\boldsymbol{E}} := \boldsymbol{I} - \left(\boldsymbol{I} + \bar{\boldsymbol{D}}\right)^{-1}. \tag{20}$$

As all detector pixels belonging to one bin share the same constant value in the upscaled stray light vector, the correction procedure may lead to visible artifacts at the bin boundaries in the stray light corrected data. These artifacts can be easily mitigated with a 2-D Gaussian filter f applied to an upscaled stray light vector. We can then express the stray light correction as

$$\boldsymbol{y}_{\mathrm{ib}} \approx \boldsymbol{y}_{\mathrm{meas}} - f\left(\boldsymbol{B}^+ \bar{\boldsymbol{E}} \cdot \bar{\boldsymbol{y}}_{\mathrm{meas}}\right). \tag{21}$$

Equation (21) has two significant computational advantages compared to a direct implementation of (5): First, the precomputed stray light extraction matrix $\bar{\boldsymbol{E}}$ is of reduced size and thus consumes less memory than its full-resolution counterpart $\boldsymbol{D}$. Second, the binning operations can be implemented

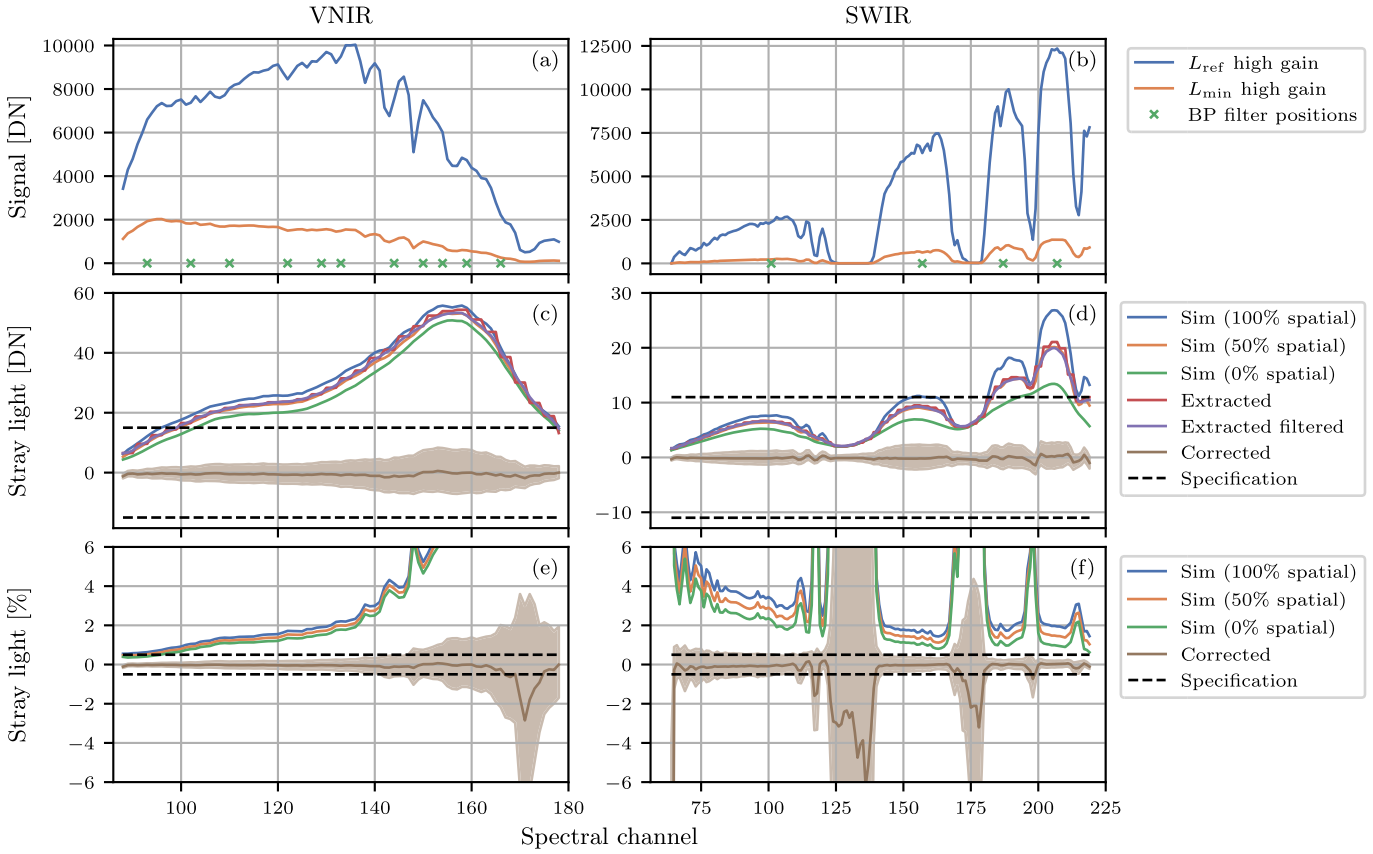

Fig. 11. Simulation results based on the stray light reference scene for (a), (c), and (e) the VNIR and (b), (d), and (f) the SWIR spectrometer. (a) and (b) EnMAP minimum L_{min} and reference L_{ref} signal levels with SLTS bandpass filter positions. (c) and (d) Simulated absolute stray light signal, which is then extracted, filtered, and corrected. The filled area indicates the maximum correction error caused by PSF uncertainties, excluding the spatial stray light uncertainty. (e) and (f) Relative stray light amount after simulation and after correction. Note that for the SWIR spectrometer, the wavelength decreases as the channel index increases.

with linear computational complexity $O(n)$ in big O notation, i.e., without matrix multiplication, while the complexity of the matrix–vector multiplication is $O(n^2)$. Also, the filter function can be implemented efficiently, whereby the optimum algorithm must be selected depending on the data and kernel size. Thus, using a smaller matrix can result in significantly improved performance.

I. Diffuse Stray Light Extraction Matrix Calculation

We perform the following procedure for the VNIR and SWIR spectrometers.

To calculate the SDF matrix $\boldsymbol{D}$, we use (1). Following Section III, we define an in-band area of 9×9 pixel^2, symmetrically placed at the PSF centers. Since we do not have a PSF measurement for each pixel i, we fill empty entries of the matrix $\boldsymbol{D}$ using a two-step process. First, we fill all entries of the channels that have PSF data using nearest neighbor interpolation, i.e., we copy the matrix entries of the closest actually measured PSFs in the same channel. In a second step, we fill the missing matrix entries of each spatial column with the closest entries in the same spatial column. This means that we also use the data copied in the first step as a reference in the second step to fill in the missing data.

The binned stray light extraction matrix $\bar{\boldsymbol{E}}$ is then calculated using (20) binning 3×3 pixel^2 for each averaged pixel with the appropriately defined matrix $\boldsymbol{B}$. The condition number of the $[\boldsymbol{I} + \bar{\boldsymbol{D}}]$ is for both, the VNIR and SWIR spectrometers, close to 1. Since the size of $\bar{\boldsymbol{E}}$ is approximately nine times smaller than $\boldsymbol{D}$, this results in a theoretically $9^2 = 81$ times faster matrix-vector multiplication.

J. Diffuse Stray Light Correction

The stray light for each measured frame is corrected following (21), where the Gaussian smoothing filter has a standard deviation of one pixel.

K. Diffuse Stray Light Simulation

To obtain the stray light impact on the stray light reference scene, we apply the SDF matrix $\boldsymbol{D}$ on the reference scene $\boldsymbol{y}_{\text{ib}}$ according to (4), which yields the stray light scene $\boldsymbol{y}_{\text{meas}}$, see Section III. We then correct the stray light follow the scheme in Section V-J. For both instruments, we simulate the stray light distribution in a scenario where the whole detector is operated in high gain mode.

L. Diffuse Stray Light Simulation Results

The results of the stray light simulations are depicted in Fig. 11. Fig. 11(a) and (b) shows the EnMAP minimum L_{min} and reference L_{ref} signal levels that compose the reference scene, see Section III.

1) VNIR Diffuse Stray Light Simulation Results: Fig. 11(c) depicts the absolute VNIR spectrometer stray light signal. We can see that the stray light signal increases with channel index, i.e., with wavelength, up to channel 159, and decreases from there. This is expected, since the VNIR PSF widths increase also with channel index, see Section V-C. The absolute stray light signal is at most 55 DN. Also, the improvement of the extracted stray light by applying a Gaussian filter is visible, as it follows the shape of the simulated stray light better. After correction, the residuals between the reference in-band signal and the stray light correction signal are below 2 DN.

The relative stray light signal increases also toward higher channel indices, see Fig. 11(e). It reaches almost 40% of L_{min} in channel 171 (not shown). After correction, the residuals are within 0.2% of L_{min} for most channels, while being with >2.5% of L_{min} at channel 171 out of the specification of 0.5%. Although the absolute residual after correction is within specification, the small L_{min} signal in this channel leads to the large relative error.

2) SWIR Diffuse Stray Light Simulation Results: For the SWIR spectrometer, the absolute stray light signal increases also toward higher channel indices, which means toward smaller wavelengths, see Fig. 11(d). For most parts of the spectral range, the stray light is within specification even without correction. Only between channels 151 and 165 for the 100% spatial stray light case, and above channel 181, the stray light is out of specification, with up to 26 DN in channel 206. The residuals of the corrected stray light are within ±1.5 DN, except for channel 199, where the correction error is 3.6 DN. This is caused by the position of the binning pattern, which we can see by comparing the extracted scattered light with the simulated one.

The relative stray light signal decreases with increasing channel index numbers, except for the spectral regions where strong atmospheric absorption in L_{ref} and L_{min} is present, see Fig. 11(f). Before correction, the relative stray light signal is up to 100% of L_{min} (not shown). After correction, the residuals are out of the relative specification of 0.5% at the end of the wavelength range and at the location of strong atmospheric absorption features. Although the absolute residuals after correction are within specification, the small L_{min} signals in these channels lead to the large relative errors.

M. Diffuse Stray Light Correction Uncertainty

Both the uncertainties of the measured PSFs and the uncertainty of the correction method have an influence on the final correction uncertainty. The uncertainty of an HDR PSF is the combination of the following uncertainties: detector effects, like pedestal offset and small signal nonlinearity, SLTS ND-filter transmission, FAI stray light, SNR, RNU, and interpolation uncertainty. The greatest uncertainty of the method is mainly due to the use of a binned stray light extraction matrix.

1) Detector Effects: To estimate the maximum systematic error caused by effects like pedestal offset and small signal nonlinearity, we calculate the ratios of consecutively scaled sub-PSFs as

$$\text{ratio}_{\text{i}} = \frac{1}{n}\sum_{j=0}^{n-1}\frac{\text{subPSF}_{i,j}}{\text{subPSF}_{i-1,j}} \qquad j = \begin{cases} 0,\ldots,n \\ \notin \text{mask}_i \\ \notin \text{mask}_{i-1} \end{cases} \tag{22}$$

where i is the sub-PSF index, j is the pixel index, and n is the total number of pixels. Masked pixels are not taken into account. For each bandpass filter, we calculate the average ratios in this manner and determine for each spatial position the maximum ratio. These ratios are then averaged for each bandpass filter to get an estimation of the maximum PSF error. The maximum error for all bandpass filters of the VNIR detector ranges from 11% to 15% (channel indices 93, 102, 110, 122, 129, 133, 144, 150, 154, 159, and 166). For the SWIR detector, the maximum error highly depends on the detector location and is with increasing channel index 19%, 27%, 17%, and 10% (channel indices 101, 157, 187, and 207). These are upper bound values, since we use the highest values of all ratios of each single PSF. Additionally, we are comparing signal values with small signal values for which the nonlinearity is much larger. Since we use the larger signal value to construct the PSFs when more than one value per pixel is usable, the actual error is expected to be much smaller.

2) ND-Filter Transmissions: The ND-filter transmission uncertainty of 2%, see Section IV, affects directly the PSF uncertainties.

3) FAI Stray Light: As discussed in Section V-E, we can estimate the portion of the PSFs that is caused by stray light originating before the FSSA. However, the stray light amount that comes from the FAI is unknown. We assume therefore that 50% of the spatial stray light is caused by the FAI. This assumption is addressed with an uncertainty of 50% of the assumed spatial stray light.

4) Signal-to-Noise Ratio: For most parts of a PSF, we use pixels with at least an SNR of > 10. However, since stray light is an additive effect, i.e., the sum of the wing signals of many PSFs at one pixel, the impact of the PSF SNRs on the noise of the extracted stray light is negligible compared to the previously discussed effects.

5) Response Non-Uniformity: The uncertainty of the RNU correction applied to all sub-PSFs is <0.9% for both detectors and is therefore negligible in comparison.

6) PSF Interpolation: Since we have measured only a subset of the instrument PSFs, most PSFs are interpolated. However, along the spatial axis, the change between two adjacent PSFs is marginal compared to the PSF uncertainty, as we can see in Figs. 4(b), 5, 7(b), and 8. The same is true along the spectral axis for the VNIR spectrometer, as shown in Figs. 4(d) and 6. For the SWIR spectrometer, only the wings of the PSFs of channel 101 are almost one order of magnitude higher toward higher channel index numbers (shorter wavelengths), see Figs. 7(d) and 9. However, due to the low signal level that can be expected at this detector location, the caused stray light signal is even without correction within specification, see Fig. 11(d). We therefore assume that the interpolation errors are negligible.

7) Combined PSF Uncertainties: We can therefore conclude that the dominant stray light correction uncertainties

arise from systematic PSF uncertainties, which are FAI stray light, uncertainties due to detector effects and SLTS ND-filter transmission uncertainties.

Without the spatial stray light, the VNIR spectrometer PSFs have an uncertainty of <17% (= <15% + 2%) (detector effects + ND-filter uncertainties). These uncertainties add linearly, since they are of systematic nature. For the reference scene, the maximum uncertainty is 7.5 DN, see Fig. 11(c). The uncertainty of the spatial stray light adds 1 DN to the maximum uncertainty in the test scene.

Without the spatial stray light, the SWIR spectrometer PSFs have uncertainties ranging from 12% to 29% (=detector effects + ND-filter uncertainties). Again, these uncertainties add linearly, since they are of systematic nature. For the reference scene, the maximum uncertainty is 3 DN, see Fig. 11(d). The uncertainty of the spatial stray light adds 3.5 DN to the maximum uncertainty in the test scene.

8) Correction Method: The correction error due to binning in the stray light reference scene is <1 DN for the VNIR spectrometer and <2 DN for the SWIR spectrometer, see Fig. 11(c) and (d). Since this is insignificant compared to the total stray light signal requirements, we assume that the errors introduced by binning are negligible.

VI. Along-Track Stray Light

Any stray light correction obviously requires knowledge about the intensity and Spectral–spatial characteristics of the incident light causing it. Along-track stray light is caused by light entering the instrument outside its nominal FOV in along-track direction. Since this is in the scanning direction of the instrument, the portion of the scene causing the stray light is recorded at another point in time within the regular FOV, given that the scene is stable between the recordings and changes of the incident angle can be neglected. If these assumptions hold, then a frame can be stray light corrected with the information found in preceding and/or following frames. To obtain the along-track stray light characteristics, we use the concept of the along-track response function (AltRF), which describes the response of one or more pixels as a function of the along-track incident angle.

A. AltRF Measurements

In order to measure the AltRFs of both spectrometers, we successively move an FPT over their along-track FOV while acquiring data at each along-track position simultaneously with both instruments. Integration time and gain of each detector are chosen to optimize SNR while avoiding saturation. Overall, we conduct two different series of measurements: one to check how the AltRFs changes with across-track position and another to get a high dynamic range AltRF over a larger angular range at the central across-track position. Both measurements are performed with a rectangular FAI FPT with a size of 10 × 2 EnMAP IFOV^2 (across- × along-track).

At each spatial position, we record 100 frames with each imaging spectrometer and a matching dark signal image with closed SLTS and WiRAL shutters.

1) Along-Track Measurements Distributed Across Both Slits: The AltRFs distributed across both EnMAP slits are measured with WiRAL coupled into the FAI. We use an EQ99 plasma lamp as WiRAL light source and set the diffraction order to zero, such that broadband light is emitted. We choose this configuration, because it provides the most uniform signal distribution over the entire spectral range of both spectrometers. AltRF measurements are performed in this configuration at 28 across-track positions evenly distributed over a viewing angle of 0.1839° covering both EnMAP slits.

To reduce measurement time, we increase the along-track step widths outside the nominal slit locations, where we expect the AltRF gradient to be smaller. Specifically, we choose step widths of 0.0078°, 0.002°, and 0.0053° outside the slit positions, at the slits, and between the slits, respectively.

2) HDR Along-Track Measurements: We measure HDR AltRFs at the across-track center using the SLTS without a bandpass filter (broadband). Using SLTS ND-filters with optical density (OD) of approximately 5, 4, 3, and 2, we conduct four measurements over a range of 0.1848° with a 0.0007° step width. An additional fifth measurement is made with the OD 2 filter, covering the maximum along-track range of ∼1.2° of the FAI with a step width of 0.0026°.

B. Along-Track Stray Light Data Evaluation

The preprocessing of the along-track stray light measurements is similar but not identical to the evaluation of the diffuse stray light evaluation described in Section V-B, owing to slightly different measurement principles. Here, we basically use a continuous slice of geometric pixels including all spectral bands as a single photo diode. Additionally, we use a larger FPT and no spectral filter, such that individual pixels do not have to be overexposed to the extent required for the diffuse stray light measurements. This approach assumes the along-track stray light to be independent of the across-track angle of incidence, an assumption easily validated by comparing the AltRF measurements acquired at different across-track angles.

The following preprocessing steps are performed before computing the AltRFs.

1) Average frames of each scene and dark measurement.
2) Mask bad pixels.
3) Mask pixels above the LFWC.
4) Apply nonlinearity correction to scene and dark measurements.
5) Subtract dark signal from scene.
6) Normalize scene signal to unit integration time.

We do not apply a gain correction, since we used the same gain settings for all measurements.

Individual slices of the AltRFs are then computed as follows from the preprocessed measurements.

1) Select the pixel with the maximum signal.
2) Select all spatial columns along the (geometric) row through the maximum, which have a signal of at least 90% of the peak intensity.
3) Select all spectral channels for each selected spatial column.

4) Calculate the mean signal over the selected detector elements.

The result is a 1-D set of points as a function of along-track angle of incidence for each ND-filter and across-track angle.

Having completed the evaluation of the distributed AltRF obtained with WiRAL, we proceed with the compilation of the HDR AltRFs. To combine the individual slices into a single AltRF, we perform an overlap matching of the slices acquired with different ND filters at the center of the across-track field of view of both cameras. The overlap matching involves fitting a single linear scaling factor for each ND-filter combination, such that the respective AltRF slices show a minimal deviation in the overlap along-track-angle interval, where both measurements have sufficient SNR. An approach using the SLTS ND-filter transmissions was not feasible, as the filters broadband transmission was not calibrated.

The obtained AltRFs have to be deconvolved, as they were acquired with an FAI FPT that is approximately twice the along-track FOV in width. For the deconvolution, we assume that the AltRF can be modeled as the sum of a core AltRF ψ_0 and an additional stray light AltRF ψ_+

$$\psi = \psi_0 + \psi_+. \tag{23}$$

Here the core AltRF is a simple model for the AltRF of an ideal instrument. Our assumption is that it is a convolution of a scaled Gaussian with two normalized rectangles in the spatial dimension

$$\psi_0(x) = A\, f_{\mathrm{G}}(x) * \sqcap_{a_1}(x) * \sqcap_{a_2}(x). \tag{24}$$

We use the Gaussian $f_{\mathrm{G}} : \mathbb{R}^d \to [0, 1]$

$$f_G := \frac{\mathrm{Tr}\,\boldsymbol{\Sigma}^{-1}}{\sqrt{2\pi}^d} \exp\left[\frac{1}{2}(\boldsymbol{x} - \boldsymbol{x}_0)^T \boldsymbol{\Sigma}^{-1}(\boldsymbol{x} - \boldsymbol{x}_0)\right] \tag{25}$$

with covariance matrix Σ

$$\Sigma_{\mathrm{ij}} := \sigma_i^2\, \delta_{\mathrm{ij}} \tag{26}$$

to model imperfections in optical components. The boxcar functions $\sqcap_{2a} : \mathbb{R} \to [0, 1]$

$$\sqcap_{2a}(x) := \begin{cases} 0, & \text{if } |x| > a \\ \dfrac{1}{2a}, & \text{if } |x| \le a \end{cases} \tag{27}$$

formalize truncation and represent the along-track influence of the instrument slit and the FAI FPT.

Note that the Gaussian component of ψ_0 does not strictly decrease to zero outside the in-band area of the PSF and thus technically contributes to the stray light we want to correct. This can be corrected later by adding these values to ψ_+.

Based on simple geometric optics, we can compute the width a_2 of the FAI FPT

$$a_2 = \frac{l_{\mathrm{D}}}{f_{\mathrm{FAI}}} \approx 0.00553^\circ \tag{28}$$

where $l_{\mathrm{D}} = 0.195$ mm is the side length of the used FAI FPT and $f_{\mathrm{FAI}} = 2020$ mm is the focal length of the FAI. The remaining parameters $\boldsymbol{\chi} := (A, x_0, a_1, \sigma)$ are components of the state vector fit with the Levenberg–Marquardt algorithm described in [14]. Since the sampling points of the along-track measurements are not equally spaced, we evaluate the function in the Fourier domain by

$$\hat{\psi}_0(\nu) = A\, \hat{f}_{\mathrm{G}}(\nu)\ \mathrm{sinc}(a_1\nu)\ \mathrm{sinc}(a_2\nu) \tag{29}$$

and then compute the fast Fourier transform (FFT) before interpolating the result at the along-track angles of the measurements. This procedure minimizes the interpolation-related uncertainty, because the interpolation can be performed on an arbitrarily dense grid, determined by the size of the FFT. The least-squares fit is limited to an interval $x_0 \pm 0.01^\circ$, where we assume the influence of ψ_0 on the total AltRF ψ to be dominant. Once a suitable set of parameters for the components of the state vector is found, the stray light AltRF is obtained as a result of the equation

$$\psi_+(x) = \psi(x) - \psi_0(x) \tag{30}$$

at the measured data points. To avoid steps at the center, we interpolate ψ_+ linearly in the fit-interval before computing its frequency spectrum $\hat{\psi}_+$ by FFT. In order to obtain the deconvolved AltRF

$$\bar{\psi}(x) = \bar{\psi}_0(x) + \bar{\psi}_+(x) \tag{31}$$

we have to compute the deconvolution of its components. The deconvolution of the core AltRF is straightforward, as it can be computed analytically in the Fourier domain

$$\mathcal{F}\{\bar{\psi}_0\}(\nu) = A\, \hat{f}_G(\nu)\ \mathrm{sinc}(a_1\nu). \tag{32}$$

The deconvolution of the stray light component is computed using the Wiener Pseudo-inverse sinc^+ of the sinc

$$\mathcal{F}\{\bar{\psi}_+\}(\nu) = \mathrm{sinc}^+(a_2\nu)\, \hat{\psi}_+(\nu) \tag{33}$$

where

$$\mathrm{sinc}^+(a_2\nu) = \frac{\mathrm{sinc}(a_2\nu)^*}{\mathrm{sinc}(a_2\nu)^*\ \mathrm{sinc}(a_2\nu) + \alpha^{-1}}. \tag{34}$$

α is a regularization term roughly equivalent to the SNR, which we estimated to be $\alpha = 2$ for this study.

C. Along-Track Response Functions

1) AltRF Distributed Across EnMAP Slits: The results of the AltRF measurements at 28 across-track positions are shown in Fig. 12(a) and (b). A deconvolution was not performed, due to the sparse spacing of the sampling points. In the dynamic range of the measurement, all AltRFs are similar and no relevant differences are visible. We can therefore assume that the AltRF is constant and does not depend on the across-track position.

2) High Dynamic Range AltRF: Fig. 12(c) depicts the measured and deconvolved AltRFs functions of the VNIR and SWIR spectrometers. The deconvolution is limited to $\pm 0.2^\circ$ from the centers, due to the increasing noise of the measured AltRFs. The dynamic range is $\sim 10^7$ for both deconvolved AltRFs, while the relative stray light amount is 0.12% (VNIR) and 0.20% (SWIR). These AltRFs are the sum of the spatial stray light originating from the FAI and from the TMA. As for the spatial component of the diffuse stray light measurements, see Section V-E, we cannot separate the stray light into its FAI and EnMAP TMA components. It is therefore again an upper limit of the along-track stray light contamination.

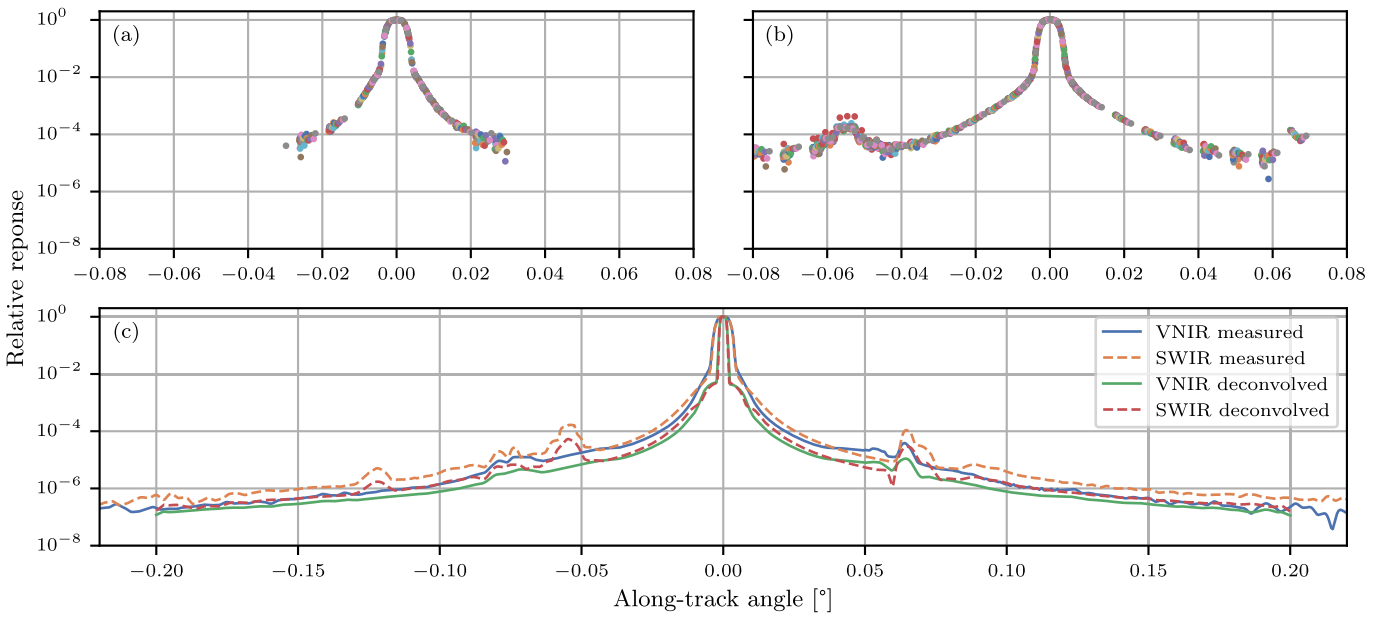

Fig. 12. AltRFs with their maxima shifted to origin. All data points of (a) VNIR and (b) SWIR AltRFs that were measured at 28 across-track positions. (c) Measured and deconvolved center HDR AltRFs.

D. Along-Track Stray Light Simulation

To simulate the impact of the along-track stray light on the stray light reference scene, see Section III, we sample the deconvolved AltRFs $\bar{\psi}$ every 9.476 arcsec, which corresponds to the ground sampling distance, by

$$z_i = \bar{\psi}(\alpha_i) \tag{35}$$

$$\alpha_i = -720.176, -710.700, \ldots, -9.476, 0, 9.476, \ldots, 710.700, 720.176\,[\text{arcsec}]. \tag{36}$$

In complete analogy to the diffuse stray light AltRFs, we define the in-band area IB $= \{-4, \ldots, +4\}$, where $i = 0$ is the location of the maximum at $\alpha_{i=0} = 0°$. Using the along-track stray light vector

$$z_{\text{sl},i} = \begin{cases} z_i, & \text{for } i \notin \text{IB} \\ 0, & \text{for } i \in \text{IB}. \end{cases} \tag{37}$$

With the along-track stray light vector $\boldsymbol{z}_{\text{sl}}$, we calculate the stray light amount of a frame $\boldsymbol{y}_j$, with j as the along-track frame index, by

$$\boldsymbol{y}_{\text{sl},j} = \sum_{i=-n/2}^{n/2-1} z_{\text{sl},i}\, \boldsymbol{y}_{\text{ib},i+j} \tag{38}$$

where n is the number of discrete along-track angles α_i. Using this approach, we determine the stray light at the evaluation point of the stray light reference scene.

E. Along-Track Stray Light Simulation Results

For the VNIR spectrometer, the absolute simulated along-track stray light is below 10 DN, see Fig. 13(a). The SWIR spectrometer stray light is for channel index <184 below the specification of 11 DN, see Fig. 13(b). For higher channel indices, the along-track stray light raises up to 18 DN. While the absolute stray light ranges from 0.3% to 0.8% (VNIR) and 0.2% to 2.0% (SWIR). As discussed in Section VI-C, the results are an upper limit for the expected along-track stray light.

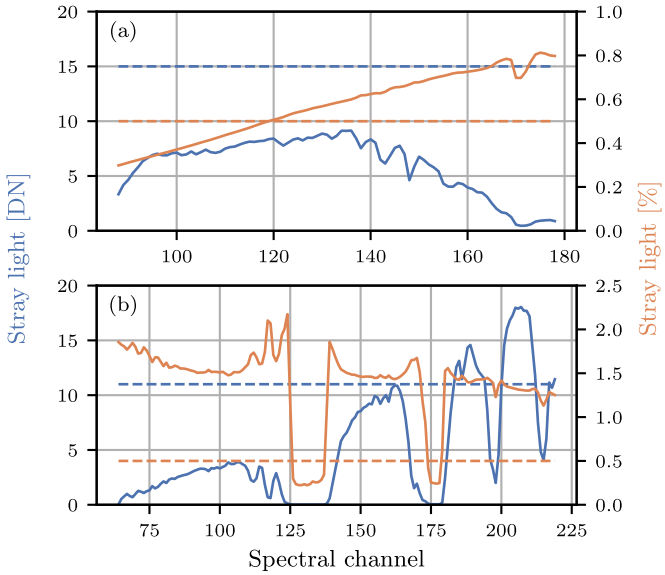

Fig. 13. Simulated along-track stray light of (a) VNIR and (b) SWIR spectrometers at the reference point of the stray light reference scene. The dashed lines indicate the maximum stray light specification. Note that for the SWIR spectrometer, the wavelength decreases as the channel index increases.

F. Along-Track Stray Light Correction

The correction is analog to the simulation method described in Section VI-D. If we apply the along-track stray light vector on a set of measured frames, we can determine the stray light amount of a frame $\boldsymbol{y}_{\text{meas},i_{\max}}$ using (38) by

$$\boldsymbol{y}_{\text{sl},j} = \sum_{i=-n/2}^{n/2-1} z_{\text{sl},i}\, \boldsymbol{y}_{\text{meas},i+j}. \tag{39}$$

We assume here that the error of using the frames already contaminated with along-track stray light $\boldsymbol{y}_{\mathrm{meas}_i}$ instead of $\boldsymbol{y}_{\mathrm{ib}_i}$ is negligible. This assumption is valid, as the simulations in Section VI-E show. Even for the high contrast in the stray light reference scene, the maximum correction error due to this assumption is 2%.

The correction is then straightforward

$$\boldsymbol{y}_{\mathrm{ib},i} = \boldsymbol{y}_{\mathrm{meas},i} - S\boldsymbol{y}_{\mathrm{sl},i} \tag{40}$$

where S is a scaling parameter to address the FAI stray light. Although uncertainties due to nonlinearity effects have an influence on accuracy of the AltRFs, the dominant uncertainty is the unknown FAI stray light contribution, which can be anything between 0% and 100% of the simulated stray light in Section VI-E.

With the available measurement equipment, it was not possible to determine the parameter S. Since we carried out the presented work before the launch of EnMAP, our intention was that the optimal parameters would be found during EnMAP's commissioning phase. However, it was decided that the impact of the along-track stray light is negligible and no correction is performed in EnMAP's processing chain at the time of writing.

VII. Summary and Conclusion

In this article, we reported the diffuse and along-track stray light calibration of EnMAP's imaging spectrometers and proposed correction methods for both types. We used the self-developed SLTS to obtain unsaturated and saturated measurements, which we combined to HDR diffuse stray light PSFs and AltRFs. This data was then used to perform simulations to estimate the impact of both stray light types.

We determined the diffuse stray light PSFs at 12 spatial and 15 (11 VNIR, 4 SWIR) spectral positions with a dynamic range between eight and nine orders of magnitude. The uncertainties of the VNIR PSFs range from 13% to 17%, while the SWIR PSFs uncertainties are 19%, 29%, 19%, and 12%. Not taken into account is the unknown stray light of the FAI, i.e., the calibration equipment. Using masked detector regions, we were able to make an educated guess of the stray light originating before the spectrometer slits, which is the sum of the FAI and EnMAP's TMA stray light. With this information, we calculated three different versions of each PSF, where we attributed 100%, 50% (used for further evaluations), or 0% of the before slit stray light to the FAI and removed it.

Although expected, we could not observe any etaloning effects in the VNIR PSFs. For both spectrometers, the principal PSF shapes are stable along the spatial axis. The VNIR PSF widths increase with the channel index, while changes between adjacent PSFs are still marginal compared to their uncertainty. On the other hand, the PSFs in the center of the SWIR spectrometer's spectral range are narrower compared to the PSFs at the beginning and end. Because only four SLTS filters were available in the SWIR region, their position was chosen to be in the middle of four spectral regions separated by atmospheric absorption bands, which are present in typical top-of-atmosphere spectra. We have assumed that each measured PSF is representative of its spectral region. This allowed us to use a modified nearest neighbor interpolation approach to derive unmeasured PSFs by interpolating first along the spectral axis and then along the spatial axis. From these PSFs, we computed a binned stray light extraction matrix with 3×3 pixel^2 tiles.

The simulations showed that in the case of the stray light reference scene, the diffuse stray light needs to be corrected. For the VNIR spectrometer, the diffuse stray light is up to 55 DN (specification $<$15 DN). The diffuse stray light of the SWIR spectrometer is between channel 181 ($\sim$1326 nm) and 219 ($\sim$900 nm) up to 26 DN (specification $<$11 DN). Using the stray light extraction matrix, the diffuse VNIR stray light can be corrected to $<$2 DN with an uncertainty of 7.5 DN (excluding FAI stray light). The correction error for the SWIR spectrometer is within $\pm$1.5 DN with an uncertainty of $\leq$3 DN, except for one channel. We assumed that the FAI stray light was removed with an uncertainty of 50% of the PSFs, resulting in additional uncertainties of at most 1 DN (VNIR) and 7.5 DN (SWIR) in the corrected reference scene.

For the along-track stray light, we found that the AltRFs are independent of the across-track position. Hence, one AltRF per spectrometer is sufficient to describe this instrument property. The determined AltRF has a dynamic range of $\sim 10^7$ over an angular range of $\pm 0.2^\circ$ with a stray light fraction of 0.12% (VNIR) and 0.20% (SWIR). Applied on the stray light reference scene, the VNIR along-track stray light is $<$10 DN (specification $<$15 DN). For the SWIR spectrometer, it is $<$11 DN up to channel 184, while for higher channel indices (shorter wavelengths), the along-track stray light increases up to 18 DN. Since the impact of the FAI stray light is unknown, we consider these results as upper limits. To adjust this impact, we have introduced a tuning parameter to the correction formula, which was to be found during the in-orbit commissioning phase of EnMAP.

While small signal linearity is relevant for the measurement of both stray light types, especially the diffuse stray light PSF measurements are demanding on detector behavior under saturation. This can be seen in the PSF uncertainties, which are dominated by detector effects, besides the unknown stray light of the FAI. For this reason, the detector requirements that arise from the stray light calibration of imaging spectrometers are usually more demanding than for operational use. This means that stray light measurements need to be considered during the specification of instrument requirements and detector effects need to be characterized to an extent that is usually not required for normal operation.

During EnMAP's commissioning phase, it was decided based on in-orbit test measurements to use the proposed diffuse stray light correction in the operational level-1 processor with the extraction matrix that has 50% of the estimated before slits of stray light are removed. In contrast, correcting the along-track stray light was not considered necessary.

Acknowledgment

The authors would like to thank Johannes Brachmann, Charles Pope, and Malte Kretz for their contribution to the SLTS development.

REFERENCES

[1] L. Guanter et al., "The EnMAP spaceborne imaging spectroscopy mission for Earth observation," *Remote Sens.*, vol. 7, no. 7, pp. 8830–8857, Jul. 2015, doi: 10.3390/rs70708830.

[2] T. Storch et al., "The EnMAP imaging spectroscopy mission towards operations," *Remote Sens. Environ.*, vol. 294, Aug. 2023, Art. no. 113632, doi: 10.1016/j.rse.2023.113632.

[3] L. Polz, A. Serdyuchenko, M. Lettner, M. Mücke, and S. Fischer, "Setups for alignment and on-ground calibration and characterization of the EnMAP hyperspectral imager," *Proc. SPIE*, vol. 11852, Jun. 2021, Art. no. 118526B, doi: 10.1117/12.2600240.

[4] S. Baur et al., "Pre-flight calibration and characterization of the EnMAP sensor," *Proc. SPIE*, vol. 12777, Jul. 2023, Art. no. 127774V, doi: 10.1117/12.2690893.

[5] G. M. Huber et al., "An all-silicon, high precision double-slit device for hyperspectral imager EnMAP," *Proc. SPIE*, vol. 11180, Jul. 2019, Art. no. 1118011, doi: 10.1117/12.2535956.

[6] B. Sang et al., "The EnMAP hyperspectral imaging spectrometer: Instrument concept, calibration, and technologies," *Proc. SPIE*, vol. 7086, Aug. 2008, Art. no. 708605, doi: 10.1117/12.794870.

[7] D. Hübner et al., "Infrared focal plane detector modules for space applications at AIM," *Proc. SPIE*, vol. 8542, Nov. 2012, Art. no. 854207, doi: 10.1117/12.2009042.

[8] C. E. Pope and A. Baumgartner, "Light source for stray light characterisation of EnMAP spectrometers," *Proc. SPIE*, vol. 11151, pp. 452–459, Oct. 2019, doi: 10.1117/12.2531264.

[9] M. Kretz, "Design and construction of a light source setup for stray light measurements in array spectrometers," M.S. thesis, KIT Karlsruhe, Karlsruhe, Germany, 2018. [Online]. Available: https://elib.dlr.de/119041/

[10] M. Lettner, T. Lamour, L. Polz, W. Glastre, E. Compain, and S. Fischer, "Versatile full aperture illumination ogse setup for alignment and end-to-end calibration of the enmap hyperspectral imager," *Proc. SPIE*, vol. 11180, pp. 2287–2303, Jul. 2019, doi: 10.1117/12.2536148.

[11] Y. Zong, S. W. Brown, B. C. Johnson, K. R. Lykke, and Y. Ohno, "Simple spectral stray light correction method for array spectroradiometers," *Appl. Opt.*, vol. 45, no. 6, p. 1111, 2006, doi: 10.1364/ao.45.001111.

[12] A. Baumgartner and C. H. Köhler, "Transformation of point spread functions on an individual pixel scale," *Opt. Exp.*, vol. 28, no. 26, pp. 38682–38697, 2020, doi: 10.1364/oe.409626.

[13] P. Blanchard and E. Brüning, *Mathematical Methods in Physics: Distributions, Hilbert Space Operators and Variational Methods* (Progress in Mathematical Physics), vol. 26. Boston, MA, USA: Birkhäuser, 2003, doi: 10.1007/978-1-4612-0049-9.

[14] J. J. Moré, "The Levenberg–Marquardt algorithm: Implementation and theory," in *Numerical Analysis* (Lecture Notes in Mathematics). Berlin, Germany: Springer, 1978, pp. 105–116, doi: 10.1007/BFb0067700.

Andreas Baumgartner received the B.Eng. degree in mechatronics with a focus on optical engineering and the M.Eng. degree in electrical engineering and information technology from the University of Applied Sciences Deggendorf, Deggendorf, Germany, in 2008 and 2010, respectively, and the Ph.D. (Dr. rer. nat.) degree in computer science from Osnabrück University, Osnabrück, Germany, in 2021.

In 2010, he joined the German Aerospace Center (DLR), Oberpfaffenhofen, Weßling, Germany, where he heads the Optical Systems Calibration Group and is responsible for DLR's calibration laboratory for imaging spectrometers. His research interests include the calibration of imaging spectrometers, correction of imaging artifacts, and the simulation of camera systems.

Claas Henning Köhler received the Diploma degree in physics from the University of Göttingen, Göttingen, Germany, in 2006, and the Ph.D. (Dr. rer. nat.) degree from the University of Leipzig, Leipzig, Germany, in 2014.

Since 2015, he has been the Head of the Optical Airborne Remote Sensing (OpAiRS) User Service, German Aerospace Center (DLR), Weßling, Germany, which collects hyperspectral datasets for DLR scientists and their cooperation partners. From 2019 to 2021, he supported the EnMAP on-ground stray light characterization as calibration scientist. His research interests include calibration algorithms for imaging spectrometers and atmospheric remote sensing.

Simon Baur received the Diploma degree in physics from the Technical University of Munich, Munich, Germany, in 2010, and the Ph.D. (Dr. rer. nat.) degree from the Max-Planck-Institute of Quantum Optics, Garching, Germany, in 2014.

In 2017, he joined OHB System AG, Weßling, Germany, as a Calibration Engineer for the on-ground testing and in-orbit commissioning of the EnMAP hyperspectral imager. While still supporting the EnMAP mission as the systems engineer for the space segment, he now primarily works as an Optical Instrument Architect developing next generation optical instruments for space applications.

Richard Wachter received the Diploma degree in physics from the University of Augsburg, Augsburg, Germany, in 2000, and the Ph.D. (Dr. sc. nat.) degree in astronomy from ETH Zürich, Zürich, Switzerland, in 2004.

After working in solar astronomy at Stanford University, Stanford, CA, USA, for several years, he joined OHB System AG, Weßling, Germany, in 2011. As an Expert for instrument performance and calibration at OHB System AG, he is supporting a variety of space borne Earth observation missions.

Leonhard Polz received the Diploma degree in engineering physics and the M.Sc. degree in micro- and nanotechnology from Munich of University of Applied Sciences, Munich, Germany, in 2010 and 2012, respectively, and the Ph.D. degree from the University of Jena, Jena, Germany, in 2017.

From 2012 to 2017, he was a Research Assistant with the Photonics Laboratory, Munich University of Applied Sciences. Since 2017, he has been an Optical Alignment and Test Engineer with OHB System AG, Weßling, Germany, where he is involved in the projects EnMAP, PLATO, and FORUM.

Anna Serdyuchenko, photograph and biography not available at the time of publication.